Uncertainty quantification in coronary blood flow simulations: impact of geometry, boundary conditions and blood viscosity

Sethuraman Sankaran[a], Hyun Jin Kim[a], Gilwoo Choi[b] and Charles A. Taylor[c,d☆]

[a]*Senior Computational Scientist, HeartFlow Inc., 1400, Seaport Blvd, Building B, Redwood City, CA 94063, U.S.A., Email: ssankaran@heartflow.com, jkim@heartflow.com*
[b]*Senior Biomedical Engineer, HeartFlow Inc., 1400, Seaport Blvd, Building B, Redwood City, CA 94063, U.S.A., Email: giroo@heartflow.com*
[c]*Founder, CTO, HeartFlow Inc., 1400, Seaport Blvd, Building B, Redwood City, CA 94063, U.S.A. Email: taylor@heartflow.com*
[d]*Consulting Professor of BioEngineering, Stanford University, 443 Via Ortega, Stanford CA 94305, U.S.A. Email: taylorca@stanford.edu*

Abstract

Computational fluid dynamic methods are currently being used clinically to simulate blood flow and pressure and predict the functional significance of atherosclerotic lesions in patient-specific models of the coronary arteries extracted from noninvasive coronary computed tomography angiography (cCTA) data. One such technology, $\mathrm{FFR_{CT}}$, or noninvasive fractional flow reserve derived from CT data, has demonstrated high diagnostic accuracy as compared to invasively measured fractional flow reserve (FFR) obtained with a pressure wire inserted in the coronary arteries during diagnostic cardiac catheterization. However, uncertainties in modeling as well as measurement results in differences between these predicted and measured hemodynamic indices. Uncertainty in modeling can manifest in two forms - anatomic uncertainty resulting in error of the reconstructed 3D model and physiologic uncertainty resulting in errors in boundary conditions or blood viscosity. We present a data-driven framework for modeling these uncertainties and study their impact on blood flow simulations. The incompressible Navier-Stokes equations are used to model blood flow and an adaptive stochastic collocation method is used to model uncertainty propagation in the Navier-Stokes equations. We perform uncertainty quantification in two geometries, an idealized stenosis model and a patient specific model. We show that uncertainty in minimum lumen diameter (MLD) has the largest impact on hemodynamic simulations, followed by boundary resistance, viscosity and lesion length. We show that near the diagnostic cutoff ($\mathrm{FFR_{CT}} = 0.8$), the uncertainty due to the latter three variables are lower than measurement uncertainty, while the uncertainty due to MLD is only slightly higher than measurement uncertainty. We also show that uncertainties are not additive but only slightly higher than the highest single parameter uncertainty. The method presented here can be used to output interval estimates of hemodynamic indices and visualize patient-specific maps of sensitivities.

Keywords: uncertainty quantification; coronary simulations; blood flow; fractional flow reserve

1. Introduction

Sufficient blood flow in the coronary arteries is essential for perfusing the myocardium and ensuring normal cardiac function. Atherosclerosis in the coronary arteries can obstruct blood flow and result in myocardial ischemia, or low myocardial blood flow particularly during physical activity, and may necessitate treatment with medical therapy, angioplasty and stenting or bypass surgery. The most effective test for assessing the functional significance of coronary artery disease is invasive fractional flow reserve (FFR) which is the ratio of mean pressure downstream of a coronary lesion to the pressure in the aorta under conditions of maximal hyperemia induced through the administration of adenosine to dilate the coronary microcirculation and increase coronary blood flow in a manner mimicking physical activity. Importantly, large prospective randomized-control clinical trials have demonstrated that the use of FFR in clinical decision-making can identify patients that should be treated medically [1] and those patients that benefit from revascularization using stents [2]. While FFR is the gold-standard for identifying lesions causal of ischemia, it is an invasive method requiring diagnostic cardiac catheterization and is negative in roughly half the patients that receive the test [3, 4, 5]. As a result, there has been significant motivation to develop a noninvasive test that could better identify patients who can be deferred from invasive diagnostic catheterization and those patients that would most likely benefit from this invasive procedure. Recently, a technique called $\mathrm{FFR_{CT}}$ has emerged for noninvasively predicting FFR using coronary computed tomography angiography (coronary CTA) to inform simulation studies of blood flow performed using computational fluid dynamics [6]. $\mathrm{FFR_{CT}}$ has demonstrated high diagnostic accuracy as compared to measured FFR [3, 4, 5] and has been shown to significantly reduce unnecessary diagnostic cardiac catheterizations without adverse clinical events [7], to improve the quality of life of patients receiving the test and reduce health care costs [8].

Patient-specific models of blood flow in arteries include a description of the anatomic region of interest created from image data, the mathematical equations representing the physical laws of blood flow within the region of interest and boundary conditions to define physiologic relationships between variables at the boundaries of the region of interest and the remainder of the circulation. Each of these elements can introduce uncertainty in the simulation and are discussed in turn in the following.

For modeling blood flow in the human coronary arteries, coronary CTA data provides input for the patient-specific anatomic model. Image artifacts, which can depend on imaging hardware, image acquisition protocols and reconstruction techniques and inherent patient characteristics can affect the quality of the image data and the segmentation of the coronary arteries. Owing to the reasons above, the reconstructed geometry from cCTA is an approximation of the true geometry (which is unknown), which has to be accounted for when performing blood flow simulations.

For many patient-specific simulations of blood flow, a Newtonian rheological model is used and a single viscosity value is assumed based on population averages. The effect of variations in blood viscosity from the population-based average will depend on the quantity of interest. For example, viscosity will have a direct effect on shear stress, but may or may not affect computed pressure gradients or fractional flow reserve values.

Inlet and outlet boundary conditions have a profound effect on blood flow simulations in patient-specific models. A robust strategy is to prescribe the flow rate or pressure at the

inlet and a lumped-parameter relationship between flow rate and pressure at the outlets of the patient-specific domain. In this work, for simplicity, we use a resistance model relating pressure to flow to model properties of the micro-circulation downstream of the large coronary arteries represented in the image-based model [6]. Although resistance values in each artery cannot be directly measured non-invasively, parameter values can be estimated based on form-function relationships applied to an individual patient and population-based physiologic responses. However, the true resistance remains unknown and it is necessary to account for this uncertainty in patient-specific models.

The main goal of this work is to understand the impact of uncertainties in lumen geometry (minimum lumen diameter and lesion length), boundary conditions and blood viscosity on the blood flow and pressures in the coronary artery. We investigate the relative importance of each of these model parameters and calculate the impact of these on $\mathrm{FFR_{CT}}$, in comparison with measurement variability. Finally, we perform a combined uncertainty quantification analysis where all variables are perturbed simultaneously to determine whether the uncertainty in the parameters is additive.

To accomplish this assessment of solution uncertainty, we use data-driven techniques for calculating the stochastic models. To account for uncertainty in geometry, we utilize data comparing minimum dimensions of the lumen segment from coronary CTA against invasive measurements obtained using optical coherence tomography (OCT). Uncertainty in lesion length is modeled based on variability in modeling stenoses by three different users segmenting the same image data. For modeling uncertainty in resistance values, we selected a cohort of patients whose reconstructed geometry matches invasive measurements obtained from intravasular ultrasound (IVUS) data. We then make the assumption that all of the differences between actual and measured FFR occurs due to error in modeling boundary resistance. This uncertainty model for boundary resistance is computed by fitting an empirical distribution to the observed data. Uncertainty in viscosity is modeled by fitting a distribution to viscosity calculated from measured values of hematocrit obtained in a recent clinical trial.

The differences between this work and prior work [22, 14] are (i) in the previous work, we used a machine learning surrogate for $\mathrm{FFR_{CT}}$ whereas we use the Navier-Stokes equations directly in this manuscript, (ii) uncertainties in minimum lumen diameter, lesion length, boundary resistance and viscosity are all included in this manuscript, whereas only geometric uncertainty was discussed earlier, and (iii) the input uncertainty model for all the parameters is computed using a data-driven approach.

The paper is organized as follows. In the methods section, we describe a data-driven approach for stochastic modeling of the various sources of uncertainties. We also describe the stochastic Navier-Stokes equations. In section 3, we describe the results obtained on an idealized and patient-specific model, including the computed standard deviation, confidence intervals and probability density functions. In section 4, we discuss implications of this work, including ranking of parameters based on their importance.

2. Methods:

We first describe the geometry of the system under consideration. Subsequently, we describe the Navier-Stokes equations governing blood flow and physiologic boundary conditions. Then, we describe the stochastic models used in this work for each of the variables,

namely minimum lumen diameter (MLD), lesion length, blood viscosity and boundary resistance. Then, we describe the adaptive stochastic collocation algorithm used to solve the stochastic Navier-Stokes equations.

2.1. Modeling geometry:

2.1.1. Idealized stenosis model

First, we analyze $\mathrm{FFR_{CT}}$ and flow through an idealized stenosis model. The geometry consists of a constant diameter cylindrical vessel with a focal stenosis, described by

$$d(z) = d_h(z)\left[1 - \frac{1}{2}\left[1 - cos\left(\frac{z - z_c}{\Delta}\pi + \pi\right)\right]\alpha\right], z_l < z < z_u \tag{1}$$

where d_h is the healthy diameter of the vessel, z_c is the location of the throat ($z_c = (z_l + z_u)/2$) of the stenosis, z_l and z_u are the start and end locations of the stenosis, Δ is the half length of the stenosis ($\Delta = (z_l + z_c)/2$) and α is the modeled % stenosis. For instance, a 60% stenosis would yield a diameter of $0.4d_h$ at the throat of the stenosis. We chose d_h to be 3.5 mm which is representative of a healthy coronary artery, z_l to be 17.5 mm and z_u to be 25 mm.

2.1.2. Patient-specific stenosis model:

We reconstruct a patient-specific model of the coronary arteries from coronary CTA images. The ascending aorta is first extracted and the coronary ostia identified. Next, the centerlines of the vessels of interest are extracted and the coronary lumen boundary is segmented for each vessel. Finally, the outlet boundaries are defined by trimming the model at pre-defined locations.

2.2. Navier-Stokes equations

Blood flow in the cardiovascular system is modeled herein using the Navier-Stokes equations given by

$$\begin{aligned} \rho\left(\mathbf{u}_{,t}\left(\mathbf{x},t\right) + (\mathbf{u}\cdot\nabla)\mathbf{u}(\mathbf{x},t)\right) &= -\nabla p(\mathbf{x},t) + \mu\nabla^2\mathbf{u}(\mathbf{x},t) + \mathbf{f} \quad \forall \mathbf{x} \in \Omega \\ \nabla\cdot\mathbf{u}(\mathbf{x},t) &= 0, \end{aligned} \tag{2}$$

where $\mathbf{f}$ represents all body forces, ρ denotes density, μ denotes dynamic viscosity, $\mathbf{u}$ denotes velocity, p denotes pressure, and Ω represents the patient-specific problem geometry. Finite element simulations have emerged as a powerful and robust tool to solve these equations in complex patient-specific geometries [9, 10, 11]. In the simulations performed here, the vessel walls are assumed to be rigid, and a Newtonian constitutive behavior of the fluid is assumed, with viscosity of blood of 0.04g/cm.s. and density of $1.06\mathrm{g/cm}^3$. For the idealized stenosis model a constant pressure boundary condition is applied at the inlet whereas for the patient-specific model, a parabolic velocity profile is prescribed at the aortic inlet based on a target cardiac output. The outlets are modeled using a resistance condition which couples blood pressure and flow rate at the outlet [10, 12, 13]. Fractional flow reserve is calculated as $\mathrm{FFR_{CT}}(\mathbf{x}) = \frac{P_c(\mathbf{x})}{P_{\mathtt{aorta}}}$ based on steady flow simulations where $P_{\mathtt{aorta}}$ is the mean aortic pressure and $P_c(\mathbf{x})$ is the mean pressure in the coronary artery [6].

2.3. Modeling uncertainties

2.3.1. Uncertainty in minimum lumen diameter (MLD)

Idealized stenosis model: For the idealized stenosis model, the uncertainty is modeled as originating from image resolution and/or image artifacts. Since state-of-the-art algorithms can represent the model with sub-voxel accuracy, we use an error of 0.3 mm in the radius, resulting in 0.6 mm error in minimum lumen diameter. We assume that the entire stenosis model uniformly dilates or erodes spatially, implying that the lumen diameter in the entire vessel reaches their minima and maxima simultaneously. While this results in sampling extreme configurations with much higher probability, our goal is to show that even such rigorous uncertainty modeling results in rather modest uncertainty in the clinical outcome, especially near the clinical cutoff of 0.8. For the idealized problem, the stenosis diameter given in Eq. 3 is now given by

$$d(z,\xi) == d_h(z)\left[1-\frac{1}{2}\left[1-cos\left(\frac{z-z_c}{\Delta}\pi+\pi\right)\right]\left(\alpha+\frac{\delta}{d_h(z)}\right)\right], z_l < z < z_u \qquad (3)$$

where δ is a uniform random variable with the range ± 0.3 mm and the uncertainty is assumed to be independent of the degree of stenosis, α. In other words, the uncertainty is modeled directly on the vessel size. Perturbation on the surface mesh is achieved using the method described in Sankaran et. al. [14].

Patient specific model: We model uncertainty in the MLD using data comparing the lumen segmentation extracted from coronary CTA against that obtained from an optical coherence tomography (OCT) technique as the reference standard. Specifically, image processing methods were applied to segment lumen boundaries of 97 lesions in 23 patients [15]. OCT data was co-registered with CT data, and the errors in MLD and MLA were quantified. The mean and standard deviation in error between segmented and ground-truth data was computed and a Gaussian distribution was used to model uncertainty in MLD.

2.3.2. Uncertainty in boundary resistance

Since it is not possible to measure resistance of the micro-vasculature including the effect of adenosine, we use the measured FFR on a set of patients to infer error in boundary resistance. First, we pick a set of 28 patients where the reconstructed geometry matched invasive imaging data using intra-vascular ultrasound. Second, we calculate the resistance under hyperemia conditions that would result in a match of $\mathrm{FFR_{CT}}$ to the measured FFR. Finally, we postulate that the difference between our assigned resistance [6] and the resistance calculated for $\mathrm{FFR_{CT}}$ to match measured FFR is representative of uncertainty in resistance, since these patients have low uncertainty in geometry. A log-normal probability distribution function, with the lower and upper 95% confidence bounds being 65% and 130% of the mean resistance, was found to fit the observed differences as shown in Figure 1. This was achieved by finding optimal parameters of the log-normal distribution that minimizes error entropy using Nelder-Mead algorithm. Therefore, this model is used to account for uncertainty in boundary resistance.

2.3.3. Uncertainty in blood viscosity

Hematocrit is modeled as a Gaussian random variable, based on values measured in a recent clinical trial [3]. A mean value of 45 and a standard deviation of 8 was observed, and

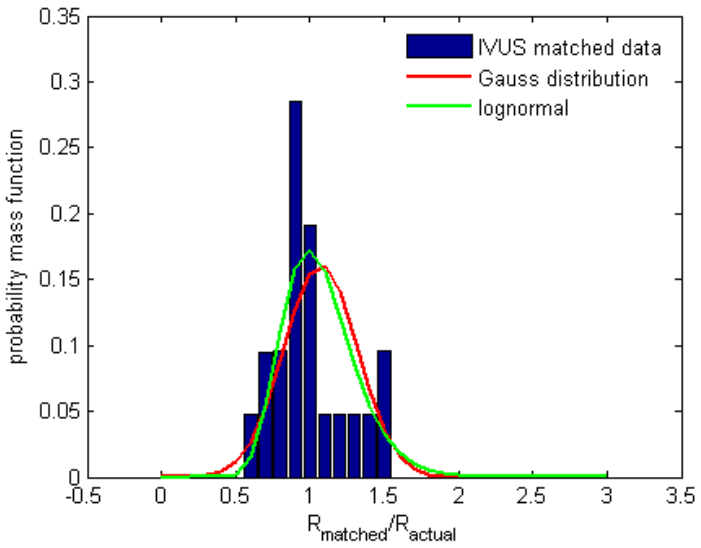

Figure 1: Histogram of the ratio of boundary resistances, where $R_{matched}$ is the resistance chosen such that FFR_{CT} matched measured FFR and R_{actual} is the resistance chosen using the method described in Taylor et. al. [6]. This histogram was only calculated for a set of patients whose reconstructed lumen diameter had a small error with respect to invasive intravascular ultrasound measurements. This histogram was hypothesized to represent the error in the modeled boundary conditions. Both a log-normal and Gaussian distribution were fit to the data, and the log-normal distribution was finally chosen since it fit the distribution better and had a lower error entropy.

hence a Gaussian distribution with these parameters was used. However, the uncertainty in viscosity (μ) varies non-linearly with uncertainty in hematocrit(hct) since they are related as

$$\mu = \frac{\mu_p}{(1 - \text{hct}/100)^{2.5}} \tag{4}$$

where μ_p, the viscosity of plasma is 0.0011 Pa.s.

2.3.4. Uncertainty in lesion length

Uncertainty in lesion length occurs due to difficulties in interpreting the extent of coronary lesions from coronary CTA data. The degree of uncertainty was generally found, based on an inter-user variability study, to be ± 1 mm, which is modeled as a uniform random variable. We show later that lesion length has the least impact on uncertainty in hemodynamics, and hence the results are not very sensitive to the model chosen.

2.4. Stochastic Navier-Stokes equations

In the stochastic version of the Navier-Stokes equations, blood velocities and blood pressures are assumed to be varying with space, time as well as a stochastic space. This is formally written as $\mathbf{u} \equiv \mathbf{u}(\mathbf{x}, t, \boldsymbol{\xi})$ and $p \equiv p(\mathbf{x}, t, \boldsymbol{\xi})$. Hence, the stochastic Navier-stokes equations are given by

$$\begin{aligned} \rho\left(\mathbf{u}_{,t}\left(\mathbf{x},t,\boldsymbol{\xi}\right)+(\mathbf{u}\cdot\nabla)\mathbf{u}(\mathbf{x},t,\boldsymbol{\xi})\right) &= -\nabla p(\mathbf{x},t,\boldsymbol{\xi})+\mu(\boldsymbol{\xi})\nabla^2\mathbf{u}(\mathbf{x},t,\boldsymbol{\xi})+\mathbf{f} \quad \forall \mathbf{x}\in\Omega^*(\boldsymbol{\xi}) \\ \nabla\cdot\mathbf{u}(\mathbf{x},t,\boldsymbol{\xi}) &= 0, \end{aligned} \tag{5}$$

These equations are solved using the adaptive stochastic collocation method [16, 18, 17]. We first compute the quadrature points where simulations will be performed, by sampling and interpolating the stochastic space using the adaptive Smolyak quadrature algorithm [17, 16, 18, 19, 20, 21]. The 3D Navier-Stokes equations are solved at each quadrature point to calculate $\mathrm{FFR_{CT}}$ [22]. Finally, we can evaluate probability distribution function of $\mathrm{FFR_{CT}}$ and confidence intervals in $\mathrm{FFR_{CT}}$ from $p(\mathbf{x},t,\boldsymbol{\xi})$.

We first perturb each of the four variables separately, fixing the others at their mean value. Then, we perform a combined uncertainty quantification analysis, whereby all the four variables are perturbed simultaneously. A four dimensional stochastic space is defined for this purpose and blood velocities and pressures at each point in space is associated with a stochastic space representation. The sensitivities (standard deviation) in $\mathrm{FFR_{CT}}$ due to the four variables are compared and ranked. Confidence intervals are also extracted. The individual sensitivities are finally compared with the sensitivities of the combined UQ model.

3. Results:

We describe the impact of uncertainty in MLD, lesion length, boundary resistance and viscosity on an idealized stenosis model first. Following this, we describe the results on a patient-specific model, which has a focal lesion in each of the main coronary vessels (left circumflex - LCx, left anterior descending - LAD and right coronary artery - RCA). Uncertainty in pressure, velocity and $\mathrm{FFR_{CT}}$ are quantified.

3.1. Idealized stenosis model

A plot of $\mathrm{FFR_{CT}}$ for different % stenoses is shown in Fig. 2. Standard deviation (both $\pm$) due to each of the variables are color coded, with MLD generally exhibiting the highest sensitivity on stenoses greater then 50%. The result of four-dimensional uncertainty quantification analysis is shown in black, and is barely visible since it is only marginally higher than the sensitivity due to MLD.

Blood pressure and velocity magnitudes along a cross-section of the idealized stenosis model are shown for six levels of disease (30% to 80% in increments of 10%) in Fig. 3. The distal pressures as well as flow-rate for each of these levels of disease are also shown. The change in pressure drop and flow-rate between, say 40% and 60% stenosis is significantly lower than between 60% and 80% stenosis. This is, in general, true for any two successive pairs of disease severity. The flow-rate in the idealized model at 80% stenosis is one-third of the flow-rate at 40% stenosis.

Blood pressure and velocity at extrema quadrature points (corresponding to $\boldsymbol{\xi}=0$ and $\boldsymbol{\xi}=1$, the minima and maxima) on an idealized model with 60% stenosis are shown in Fig. 4. The corresponding flow-rates are also listed. The largest difference in pressure drop (and hence difference in $\mathrm{FFR_{CT}}$) across the stochastic space due to MLD, lesion length, boundary resistance and hematocrit were calculated to be 29 mm Hg, 6 mm Hg, 9 mm Hg and 4 mm

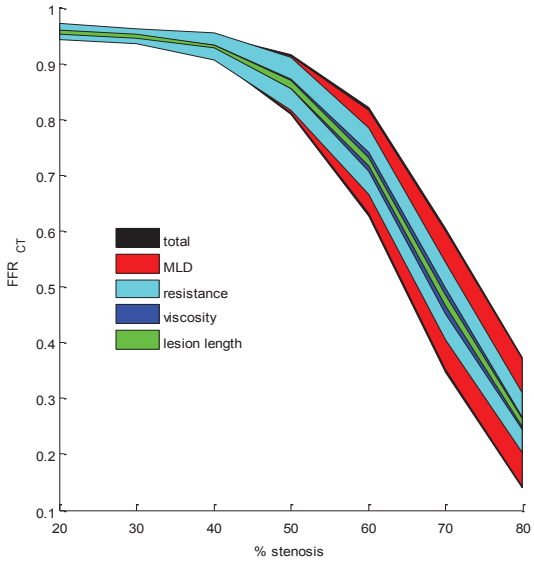

Figure 2: Fractional flow reserve calculated from CT (FFR_{CT}) for different % stenoses in an idealized arterial model. The sensitivities of FFR_{CT} to variability in the four parameters are plotted, demonstrating that the minimum lumen diameter (MLD) has the highest impact, followed by boundary resistance, blood visocity and lesion length. Further, a combined uncertainty quantification analysis results in almost a similar variability as the highest sensitive variable (MLD).

Hg respectively. The corresponding difference in flow rates were 1.3 cc/s, 0.2 cc/s, 0.9 cc/s and 0.2 cc/s. Hence, the relative importance of the four variables, quantified by their impact either on the pressure drop, FFR_{CT} or flow-rate were (in decreasing order of importance) MLD, boundary resistance, hematocrit and lesion length.

3.2. Patient-specific model

Here, we show the relative impact of minimum lumen diameter, lesion length, boundary resistance and blood viscosity on a patient specific model. Figure 5 shows the standard deviation and confidence intervals in FFR_{CT} resulting from uncertainties in MLD, lesion length, boundary resistance and viscosity respectively. The values are reported at the distal ends of each of the vessels (LAD, LCx and RCA). The figure shows that MLD has the highest impact in the LAD and LCx followed by boundary resistance, blood viscosity and lesion length. This trend was not observed in the RCA, though the magnitude of uncertainty in FFR_{CT} was generally small (less than 0.03). Further, the green lines represent reproducibility of measured FFR [23], and only uncertainty in MLD is slightly higher than measurement uncertainty.

Mean FFR_{CT} on the patient specific model is shown in Fig. 6. The mean value of FFR_{CT} in the distal ends of each of the territories, along with the confidence intervals, is also shown. Probability distribution functions of FFR_{CT} at the distal ends of LAD, LCx and RCA are shown in Fig. 6. These are obtained by sampling the stochastic space representation of FFR_{CT} corresponding to the different variables. These distributions, again, highlight the

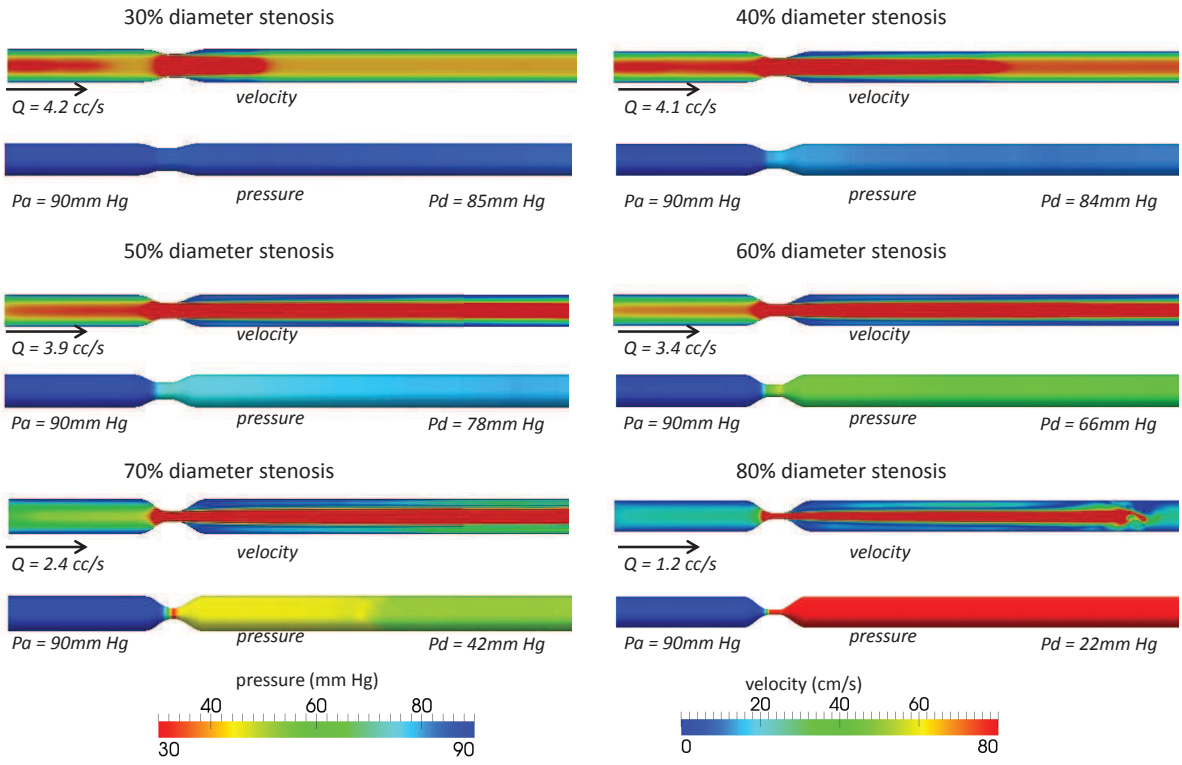

Figure 3: Pressure and velocity plots at six different levels of disease corresponding to 30%,40%,50%,60%,70% and 80% stenosis.

importance of modeling uncertainty in MLD, and demonstrates that on average the range of FFR_{CT} near the diagnostic cutoff of 0.8 is within the bounds of reproducibility of measured FFR.

Patient-specific FFR_{CT} maps, at the extrema stochastic collocation points (corresponding to $\boldsymbol{\xi} = 0$ and $\boldsymbol{\xi} = 1$), due to uncertainty in MLD in the LAD, LCx and RCA are shown in Figure 7. The locations of the MLD are also marked. Similarly, patient-specific FFR_{CT} maps corresponding to lesion length are shown in Figure 8.

4. Discussion

We applied an adaptive stochastic collocation method for analyzing the impact of uncertainty in minimum lumen diameter, lesion length, boundary resistance and blood viscosity on blood flow simulations. We showed these results on both an idealized stenosis model and a patient-specific geometry with lumen narrowing on each of the major coronary arteries (LAD, LCx and RCA).

We observed that the relative importance of uncertainty in minimum lumen diameter exceeds that of the other variables considered (lesion length, viscosity and boundary resistance). These were true in both the idealized stenosis model as well as the patient-specific

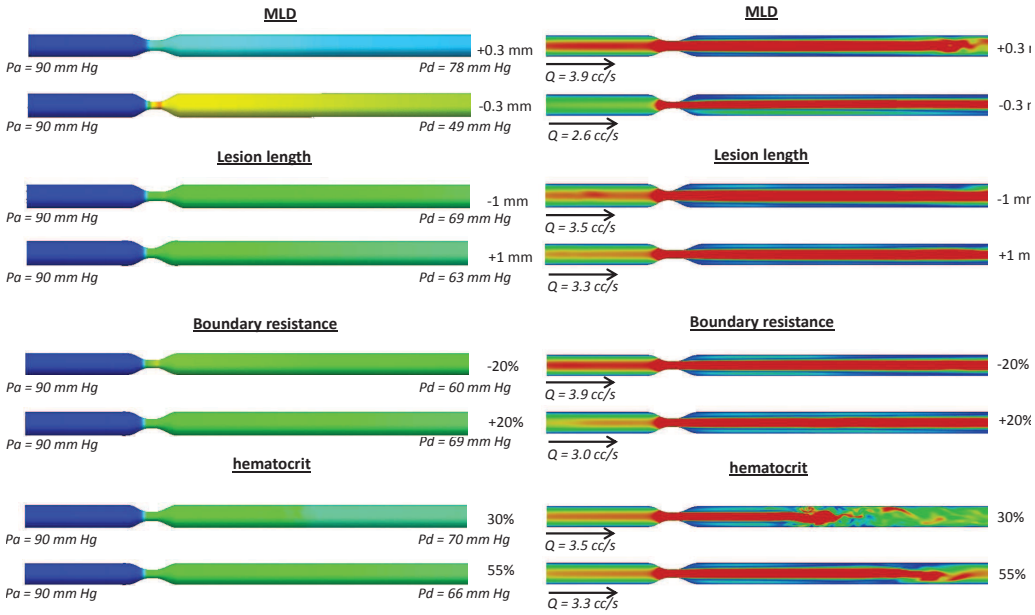

Figure 4: Simulation results for (left) pressure and (right) velocity corresponding to four different variables (from top) minimum lumen diameter(MLD), lesion length, boundary resistance, and hematocrit, shown at the extrema quadrature points in the stochastic space (minimum and maximum). The distal pressures as well as net flow rates are also listed, showing that the minimum lumen diameter has the most impact on simulation results.

geometry. For the RCA, the magnitude of uncertainty due to MLD was similar to the other factors, since the MLD in the deterministic model was not low enough (FFR_{CT} was greater than 0.8), and other factors such as boundary resistance were equally important. These are consistent with what we might expect from analytical models. The Poiseulle equation predicts pressure loss between two locations, a and b in a vessel as

$$P_a - P_b = \int_a^b \frac{8\mu Q dx}{\pi r(x)^4} \tag{6}$$

where r_a and r_b are the vessel radii at locations a and b, P_a and P_b are the corresponding blood pressures, Q is the flow-rate through the vessel and μ is the viscosity. Bernoulli's equation predicts pressure loss as

$$P_a - P_b = \frac{1}{2}\rho(v_b^2 - v_a^2) \tag{7}$$

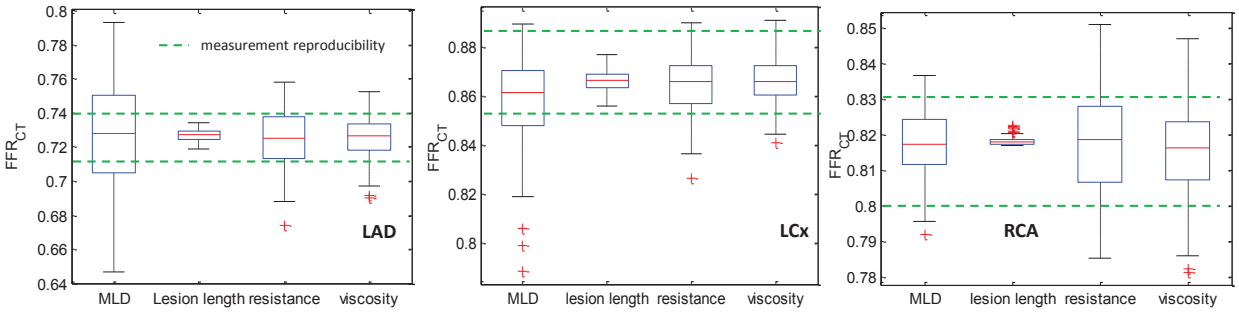

Figure 5: Comparison of standard deviation and outliers due to uncertainty in MLD, lesion length, boundary resistance and viscosity for each of the three lesions . The figure demonstrates that uncertainty in MLD generally dominates and that uncertainties in the rest of the variables are usually within reproducibility of measurements (dotted green lines representing a variation of 0.03 in measurement FFR [23]). The asymmetry in uncertainty due to minimum lumen diameter is because of the non-linear pressure drop due to changes in radii. The combined uncertainty including all four variables for LAD, LCx and RCA were 0.037, 0.023 and 0.024 respectively, which is significantly lower than their additive sums.

which can be re-written as

$$P_a - P_b = \frac{Q^2}{2\pi^2}\rho(1/r_b^4 - 1/r_a^4). \tag{8}$$

where v_a and v_b are the blood velocities at a and b. Neglecting the pressure recovery between the throat of the stenosis, c and the location b, the pressure loss can be written as

$$P_a - P_b \approx P_a - P_c \approx \frac{Q^2}{2\pi^2}\rho(1/r_c^4) \tag{9}$$

Hence, both Poiseuille's and Bernoulli's model predict that pressure loss varies with the inverse of the fourth power of MLD. However, Poiseulle's equation is linear with respect to flow rate, lesion length and blood viscosity while Bernoulli's equation is quadratic with respect to flow rate but does not depend on lesion length or viscosity.

The magnitudes of predicted uncertainty are significantly less than what one might obtain from analytical equations such as Poiseuille or Bernoulli's equation, see e.g. those predicted in [24]. The reasons are two-fold. First, it is unrealistic to assume that uncertainty in minimum lumen diameter is correlated across the entire geometry, which implies a much larger error in geometry obtained from CT scans than those reported in literature. Second, there is some self-regulation when considering uncertainty in MLD. A smaller MLD results in higher resistance to flow but also reduces the flow through that segment of the vessel. Hence the net pressure drop is lower than what one might expect assuming flow rate is the same.

Velocity contours with hematocrit changes look different compared to the other variable studies, in spite of the flow-rate and pressure drop being within the range of the other variable studies. This is due to the difference in internal shear between fluid layers resulting in a different velocity profile for the same flow rate. The difference can also be explained

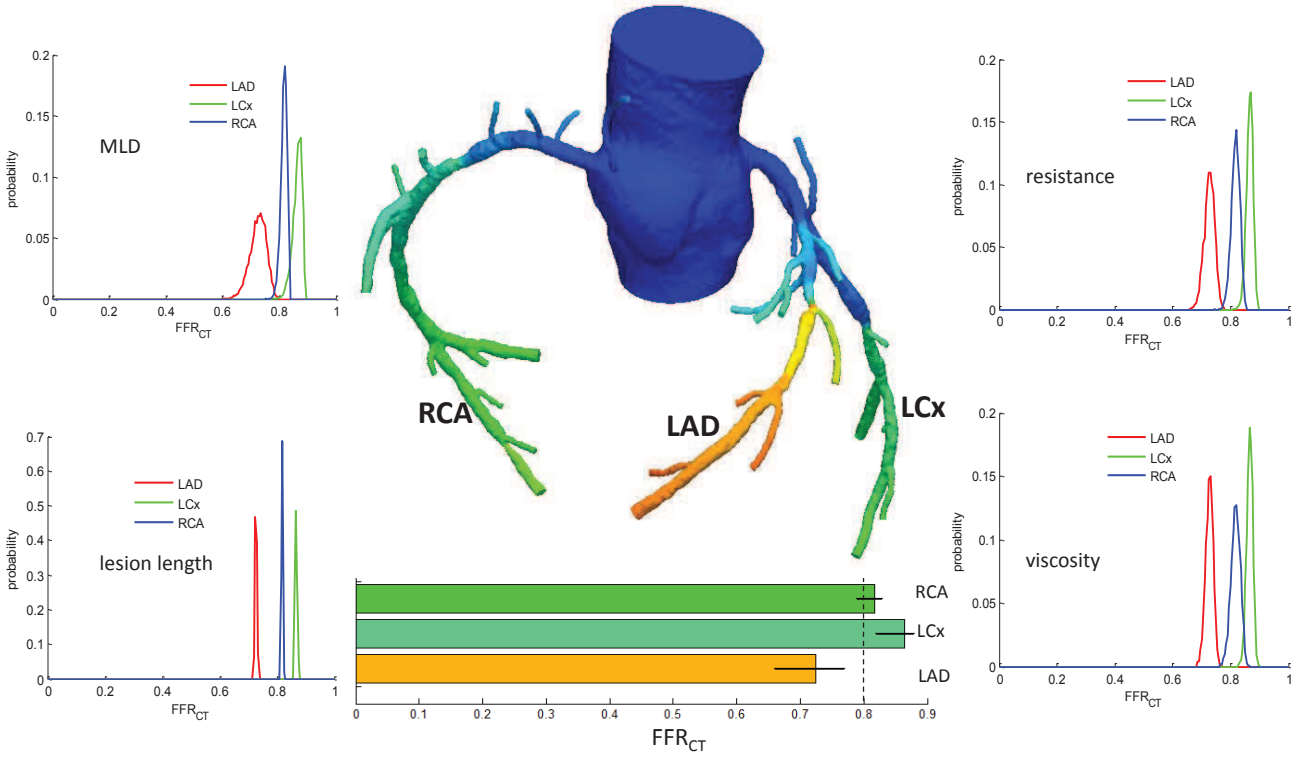

Figure 6: FFR_{CT} map computed at the mean value of all the parameters shown along with the confidence intervals for LAD, LCx and RCA (below). The figure also shows probability distribution of FFR_{CT} due to uncertainty in (from left) MLD, lesion length, resistance and viscosity in the LAD, LCx and RCA. Lesion length has the smallest magnitude of uncertainty in FFR_{CT} whereas MLD has the highest. The effect of uncertainty in boundary resistance is slightly higher than that due to uncertainty in blood viscosity.

using Reynolds number (Re). For the same velocity and characteristic diameter, $Re \propto 1/\mu$, and hence a patient in the lower limit of hematocrit can have twice the Reynolds number as a patient in the upper limit, which leads to the turbulent features and flow instabilities observed downstream of the stenosis.

Comparison of the standard deviation in FFR_{CT} resulting from uncertainty in the four variables with reproducibility of measured FFR revealed that only variability in MLD is of a similar magnitude in patient-specific models. This could be due to the factors described in the previous paragraph, but in addition, it is prudent to note that higher magnitudes of uncertainties may occur with more diseased vessels (e.g. 70 or 80% stenosis). However, they do not impact clinical diagnosis since FFR for these patients are generally much less than 0.8. Hence, we picked a patient specific example where the FFR_{CT} was near the 0.8 cutoff.

We also observed that uncertainty is not additive. In fact, analysis of the combined uncertainty of the four variables was only slightly higher than the highest uncertainty due to each variable individually. This is because the four variables are independent, and the probability of all four variables simultaneously being at their extrema is very low. Hence,

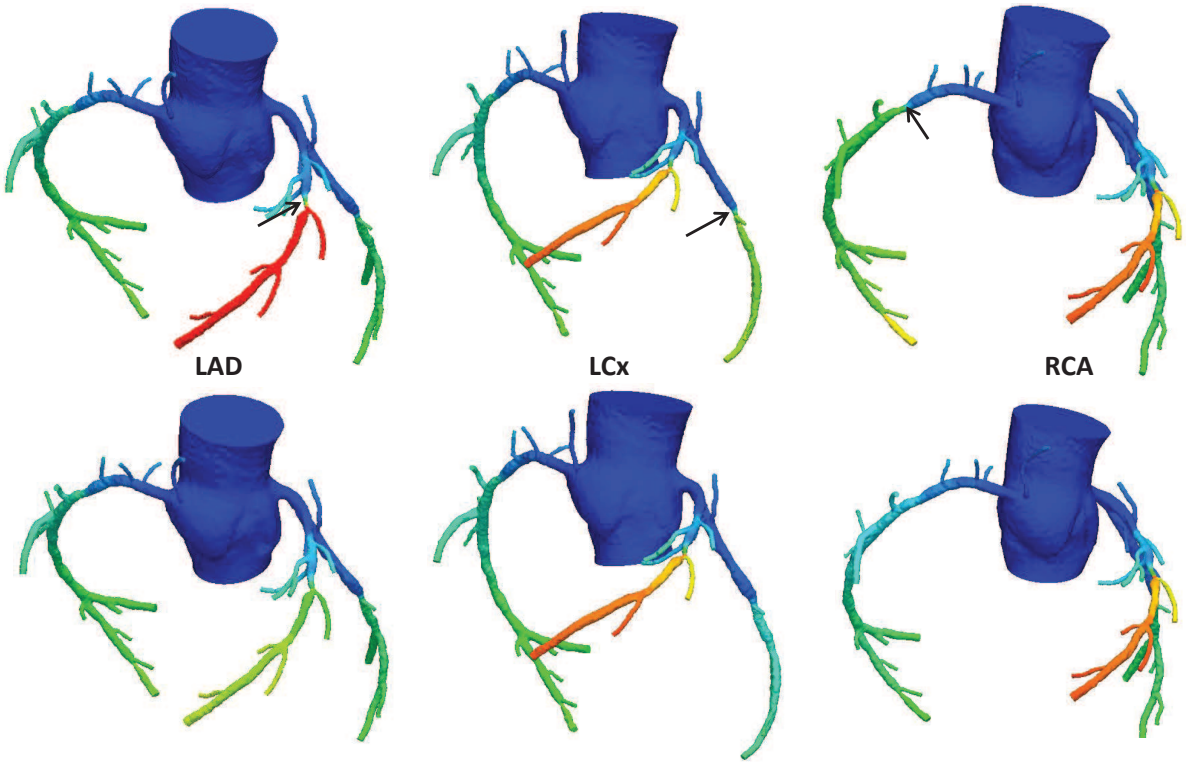

Figure 7: Uncertainty in MLD at the extrema of the stochastic space (smallest and largest sampled diameter) in (from left) LAD, LCx and RCA. The biggest difference is in the LAD where the FFR_{CT} changes from around 0.6 (diseased) to more than 0.8 (healthy). However, since these are extrema in the stochastic space, the actual standard deviation and confidence intervals in FFR_{CT} are significantly lower (as shown in the table).

when considering multiple variables, it is important to perform a multi-parameter stochastic study as opposed to combining the results of multiple single-parameter studies. In this context, the adaptive sparse grid collocation was found to be very useful in identifying optimal quadrature points in the stochastic space. We performed between 5 and 13 simulations for single parameter uncertainty quantification and between 17 and 25 simulations for the combined uncertainty quantification.

In quantifying the impact of uncertainty on simulations, it is important to identify and accurately model the underlying source of uncertainty. Uncertainty in minimum lumen diameter and lesion lengths were modeled by computing an error histogram between these values on the reconstructed geometry compared to a ground truth. Ground truth data was obtained by using invasive methods such as intravascular ultrasound or optical coherence tomography technique. However, we did not consider systolic and diastolic differences in modeling uncertainty in radius. The uncertainty model depends on the particular algorithm used to compute lumen segmentation from cCTA images. Similarly, uncertainty in viscosity was modeled by collecting inter-subject data. Uncertainty in boundary conditions was a bit

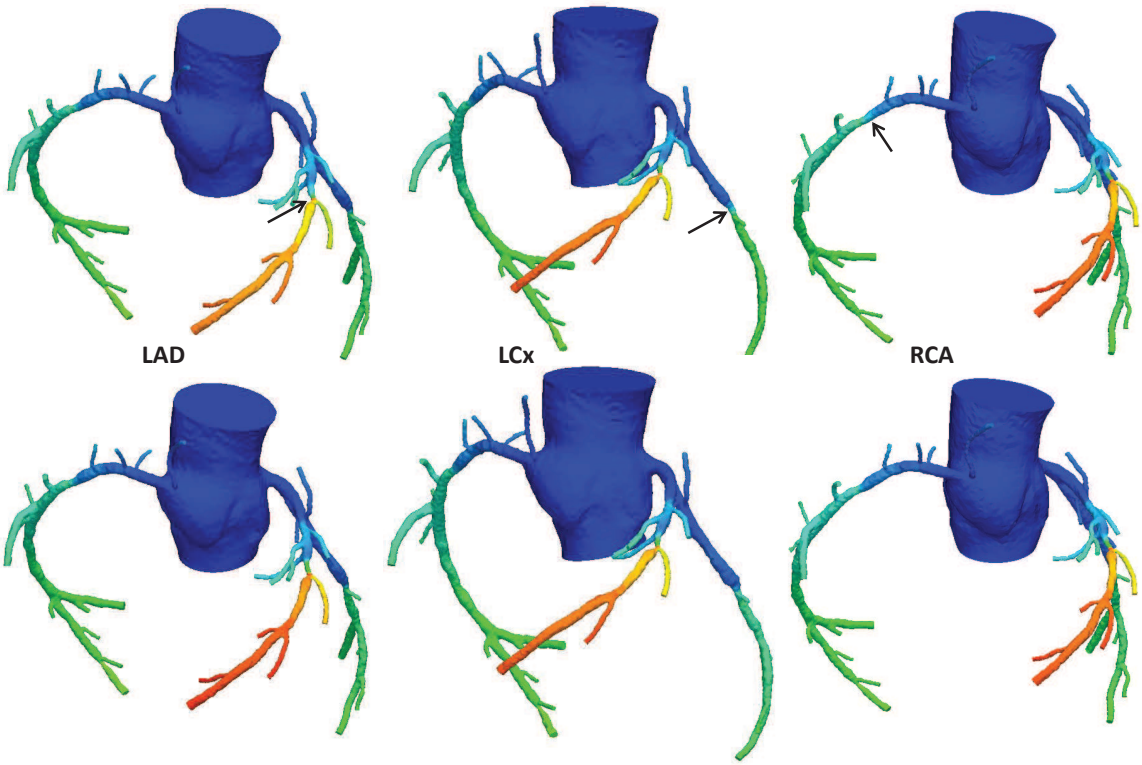

Figure 8: Uncertainty in lesion length corresponding to lengths of (top) 2 mm and (bottom) 0 mm in (left) LAD, LCx and RCA. The impact of lesion length on FFR_{CT} is minimal.

challenging, since they are not measurable directly. In this work, we assumed that ground truth boundary conditions are those that match measured pressure data within the coronary arteries, on cases with accurate geometry (validated against intra-vascular ultrasound). However, our work assumed that the patients do not have microvascular dysfunction, in which case the magnitude of uncertainty in resistance could be higher. Also, with more data, the use of a localized image quality metric to define input uncertainties would result in a more accurate assessment of geometric uncertainty.

The framework outlined herein may be useful in calculating the uncertainty in geometry, boundary conditions as well as other parameters such as viscosity in patient-specific models. This would help in reporting standard deviation and confidence intervals, and ultimately interval estimates instead of point estimates. Further, this data may help physicians understand the impact of modeling uncertainty when diagnosing functional significance of coronary artery disease in patients with equivocal diagnostic tests.

5. References

[1] Tonino P.A., B. De Bruyne, and N.H. Pijls et.al. Fractional flow reserve versus angiography for guiding percutaneous coronary intervention. *The New England Journal of Medicine*, 360:213–224, 2009.

[2] B. De Bruyne, W. F. Fearon, and N.H.Pijls et al. Fractional flow reserve-guided PCI for stable coronary artery disease. *The New England Journal of Medicine*, 371:1208–1217, 2014.

[3] J. K. Min, J. Leipsic, M.J. Pencina, D.S. Berman, B. K. Koo, C. ven Mieghem, A. Erglis, F.Y. Lin, A.M. Dunning, P. Apruzzese, M.J. Budoff, J.H. Cole, F.A. Jaffer, M.B. Leon, J. Malpeso, G.B. Mancini, S.J. Park, R.S. Schwarts, L.J. Shaw, and L. Mauri. Diagnostic accuracy of fractional flow reserve from anatomic CT angiography. *Journal of American Medical Association*, 308(12):1237–1245, 2012.

[4] B.K. Koo, A. Erglis, J.H. Doh, D.V. Daniels, S. Jegere, H.S. Kim, A. Dunning, T. DeFrance, A. Lansky, J. Leipsic, and J.K. Min. Diagnosis of ischemia-causing coronary stenoses by noninvasive fractional flow reserve computed from coronary computed tomographic angiograms results from the prospective multicenter DISCOVER-FLOW (diagnosis of ischemia-causing stenoses obtained via noninvasive fractional flow reserve) study. *Journal of American College of Cardiology*, 58(19):1989–1997, 2011.

[5] B.L. Norgaard, J. Leipsic, S. Gaur, S. Seneviratne, B. S. Ko, H. Ito, J.M. Jensen, L. Mauri, B. De Bruyne, H. Bezerra, K. Osawa, M. Marwan, C. Naber, A. Erglis, S. J. Park, E.H. Christiansen, A. Kaltoft, J. F. Lassen, H. E. Btker, and S. Achenbach. Diagnostic performance of non-invasive fractional flow reserve derived from coronary CT angiography in suspected coronary artery disease: The NXT trial. *Journal of American College of Cardiology*, 63(12):1145–1155, 2014.

[6] C.A. Taylor, T. A. Fonte, and J. K. Min. Computational fluid dynamics applied to cardiac computed tomography for noninvasive quantification of fractional flow reserve: scientific basis. *Journal of American College of Cardiology*, 61(22):2233–2241, 2013.

[7] P.S. Douglas, G. Pontone, and M.A. Hlatky et.al. Clinical outcomes of fractional flow reserve by computed tomographic angiography-guided diagnostic strategies vs. usual care in patients with suspected coronary artery disease: the prospective longitudinal trial of FFRct: outcome and resource impacts study. *European Heart Journal*, 2015.

[8] Hlatky M.A. et. al. Quality of life and economic outcomes of assessing fractional flow reserve with computed tomography angiography : The PLATFORM study. *Journal of the American College of Cardiology*, page in press, 2015.

[9] C. A. Taylor, T. J. R. Hughes, and C. K. Zarins. Finite element modeling of blood flow in arteries. *Computer Methods in Applied Mechanics and Engineering*, 158(1-2):155–196, 1998.

[10] H.J. Kim, I. E. Vignon-Clementel, J.S. Coogan, C.A. Figueroa, K.E. Jansen, and C.A. Taylor. Patient-specific modeling of blood flow and pressure in human coronary arteries. *Annals of Biomedical Engineering*, 38(10):3195–3209, 2010.

[11] K. E. Jansen, C. H. Whiting, and G. M. Hulbert. A generalized-alpha method for integrating the filtered Navier Stokes equations with a stabilized finite element method. *Computer Methods in Applied Mechanics and Engineering*, 190(3-4):305–319, 2000.

[12] K.E. Jansen I.E. Vignon-Clementel, C. A. Figueroa and C.A.Taylor. Outflow boundary conditions for three-dimensional finite element modeling of blood flow and pressure in arteries. *Computer Methods in Applied Mechanics and Engineering*, 195(29-32):3776–3796, 2006.

[13] S. Sankaran et. al. Patient-specific multiscale modeling of blood flow for coronary artery bypass graft surgery. *Annals of Biomedical Engineering*, 40(1):2228–2242, 2012.

[14] S. Sankaran, L. Grady, and C.A. Taylor. Impact of geometric uncertainty on hemodynamic simulations using machine learning. *Computer Methods in Applied Mechanics and Engineering*, 297:167–190, 2015.

[15] G. Choi et. al. Accuracy of lumen boundary extracted from coronary cta for calcified and noncalcified plaques assessed using oct data. *Journal of the American College of Cardiology*, 66(15):Suppl B, B134, 2015.

[16] D. Xiu and J. S. Hesthaven. High order collocation methods for the differential equation with random inputs. *Journal of Scientific Computing*, 27:1118–1139, 2005.

[17] S. Sankaran and A.L. Marsden. A stochastic collocation method for uncertainty quantification and propagation in cardiovascular simulations. *Journal of Biomechanical Engineering*, 133:031001–1, 2011.

[18] I. Babuska, F. Nobile, and R. Tempone. A stochastic collocation method for elliptic partial differential equations with random input data. *SIAM Journal on Numerical Analysis*, 45(3):1005–1034, 2007.

[19] A. Klimke. Uncertainty modeling using fuzzy arithmetic and sparse grids. *PhD Thesis, Universitt Stuttgart, Shaker Verlag, Aachen*, 2006.

[20] S. Sankaran and A.L. Marsden. The impact of uncertainty on shape optimization of idealized bypass graft models in unsteady flow. *Physics of Fluids*, 22:121902, 2010.

[21] S. Sankaran. Stochastic optimization using a sparse-grid collocation scheme. *Probabilistic Engineering Mechanics*, 24(3):382–396, 2009.

[22] S. Sankaran, L. Grady, and C.A. Taylor. Fast computation of hemodynamic sensitivity to lumen segmentation uncertainty. *IEEE Transactions on Medical Imaging*, in press, 2015.

[23] S. Gaur et. al. Reproducibility of invasively measured and non-invasively computed fractional flow reserve. *Journal of the American College of Cardiology*, 63(12), 2014.

[24] N.P. Johnson, R.L. Kirkeeide, and K.L. Gould. Coronary anatomy to predict physiology. *Circulation: Cardiovascular imaging*, 6:817–832, 2013.